meteorology

MDPI

Article

Meteorological Models Evaluation for Optimized Photovoltaic Power Forecasting

Ying Liu [1], Yunfei Xu [1], Kevin K. W. Cheung [2,*], Zanhua Dong [2], Zhongxin Fan [3], Lijuan Wang [3], Xiong Xiong [4], Lei Huang [1], Bitao Xiao [1] and Yuanjian Yang [2]

[1] Guodian Nanjing Automation Co., Ltd., Nanjing 210032, China
[2] School of Atmospheric Physics, Nanjing University of Information Science and Technology, Nanjing 210044, China
[3] National Demonstration Center for Experimental Atmospheric Science and Environmental Meteorology Education, Nanjing University of Information Science and Technology, Nanjing 210044, China
[4] School of Automation, Nanjing University of Information Science and Technology, Nanjing 210044, China
* Correspondence: kevin.cheung@nuist.edu.cn

Abstract

Accurate meteorological forecasts are critical for optimizing photovoltaic (PV) power generation, yet the performance of numerical weather prediction (NWP) models at specific power plant sites remains underexplored. This study evaluates four meteorological models—a commercial model (named GD), the NUIST regional model, the European Centre for Medium-range Weather Forecasts-Integrated Forecast System (ECMWF-IFS), and the German Weather Service ICOsahedral Nonhydrostatic-seamless (DWD ICON-seamless) model—against 15-min observational data from three PV sites in China (coastal low-altitude ZJ, inland low-altitude JX, and high-altitude QH) over periods spanning 2023–2025. Standard error metrics (mean bias, mean absolute error or *MAE*, root-mean-square error or *RMSE*, index of agreement or *IOA*, and correlation) are applied to 10-day forecasts of surface pressure, temperature, humidity, wind, and 6-h forecasts of solar radiation components. The NUIST model substantially outperforms GD in 2-m temperature at QH (*MAE* reduction of ~52%) and in 10-m wind speed at ZJ (*MAE* reduction of ~16%), while GD shows slight advantages in wind speed at inland sites and in wind direction bias. For ultrashort-term solar radiation, the ICON model consistently achieves the lowest *MAE* for total shortwave radiation across all sites, with a 26.8% reduction at ZJ compared to GD. All models exhibit systematic temperature underestimation and large uncertainties in wind simulation, particularly at inland locations. These findings provide a quantitative basis for constructing optimized, site-specific ensemble forecast strategies to enhance PV power prediction.

Keywords: renewable energy; photovoltaic power forecast; optimized meteorological models; data fusion

Academic Editor: Edoardo Bucchignani

Received: 13 October 2026
Revised: 11 November 2026
Accepted: 17 November 2026
Published: 19 November 2026

Copyright: © 2026 by the author. Licensee MDPI, Basel, Switzerland. This article is an open access article distributed under the terms and conditions of the Creative Commons Attribution (CC BY) license.

1. Introduction

Renewable energy always possesses mutual influences with weather and climate systems. On one hand, renewable energy aims at reducing the hazardous impacts from using fossil fuels and thus is one of the climate change mitigation measures towards environmental sustainability [1]. On the other hand, depending on the effectiveness of such mitigation measures, the evolving climate change would affect the availability of

renewable energy resources [2,3]. In operational renewable energy production, such as through photovoltaic (PV) and wind resources, power forecasting is a critical component [4]. Skillful power forecasting not only facilitates efficient use of the PV and wind turbine hardware, but it also reduces the risk of infrastructure losses in scenarios of hazardous weather systems.

PV power forecasting involves a complex model chain [5,6], a major component of which is the meteorological driver [7]. Weather factors also drive purely statistical power estimation models (e.g., [8]) as well as machine learning-based models [9,10]. However, energy-related natural resources from the atmosphere and oceans are highly stochastic in nature [11]. Predictability of the meteorological elements, which vary enormously in terms of scales, would then impact that of every component in the model chain for power production estimation. An important strategy in evolving towards probabilistic power forecasting, such that uncertainties can be quantified, is using an ensemble of meteorological models [6]. One step further from this strategy would be to better understand the performance of individual meteorological models at specific power plants, which may not be well covered by the operational weather stations network. Only after evaluation of the models in terms of the energy-critical weather elements can an optimized data fusion strategy be developed.

Power forecasts with different lead times are all essential for efficient and smooth energy production and storage operations. Ultrashort (hourly) to short-term (sub-daily) forecasts provide assessment of whether any immediate adjustment to the power plant hardware is necessary. Medium-term (one week to month) forecasts can take advantage of synoptic weather forecasts in assessing production versus needs a few weeks ahead, as well as potential impacts from hazardous weather such as tropical cyclones. Long-term (intra-seasonal to seasonal) forecasts then provide the basis for planning energy distribution and storage. In this study, we perform an evaluation of four global and regional meteorological models based on observations collected at three major PV production plants operated by one of the national power grids in China. The focus of evaluation is on the weather elements that drive PV power forecast models. In the following, a brief literature review on the importance of meteorological forecasts to energy power estimation is presented first in Section 2. Our datasets and evaluation methodology can be found in Section 3, followed by the evaluation results for short- and medium-timescale forecasts in Section 4. Section 5 then provides further discussion on our study's limitations, our results' relevance to PV power forecasting, and an overall summary.

2. Brief Literature Review

The importance of accurate photovoltaic (PV) power forecasting extends well beyond operational dispatch. As energy communities increasingly operate under virtual net billing (VNB) schemes with battery storage and dynamic tariffs, the sizing and investment planning of PV and storage assets depend critically on reliable expectations of PV production [12]. Forecast errors translate directly into suboptimal capital allocation, missed self-consumption opportunities, and exposure to volatile pricing. This planning-level dependency establishes accurate PV forecasting as a precondition for economically sound investment decisions, not merely a real-time operational convenience.

The dependence of PV power forecasting on meteorological forecasts is structural rather than incidental, and it manifests across all major model families. Data-driven forecasting approaches, comprehensively reviewed by Iheanetu [13], rely on historical PV generation and meteorological variables (irradiance, temperature, humidity, cloud cover) as inputs, and their skill is bounded by the quality and representativeness of those meteorological predictors. Physical and hybrid approaches make the meteorological dependency even more explicit. Yang et al. [6] frame the solar power curve as the essential

https://doi.org/10.3390/meteorology5040044

mapping from irradiance and auxiliary weather variables to power, whether modeled through regression, physical model chains, or their hybridization, and they note that probabilistic extensions of these curves enable uncertainty quantification. At the upstream end of the forecasting chain, Yang et al. [14] emphasize that solar irradiance forecasting is an atmospheric process and that numerical weather prediction (NWP), forecast downscaling, aerosol representation, and cloud forecasting are indispensable ingredients of solar power forecasting. The practical consequence is that errors in the meteorological forecast propagate directly into the power forecast; model-chain approaches, while physically transparent, are explicitly sensitive to NWP errors and require detailed meteorological inputs and calibration. Accurate meteorological forecasts are therefore not a background input, but a primary determinant of PV forecast skill.

This dependency becomes more consequential as the field moves from deterministic to probabilistic forecasting. Li and Zhang [15] document that the value of probabilistic solar forecasts is increasingly recognized because solar power is variable and uncertain, and they review how probabilistic forecasts are integrated into power-system decision-making through probabilistic load flow, stochastic optimization, robust optimization, and chance constraints. Each of these applications requires well-calibrated uncertainty information, and for PV the dominant source of that uncertainty originates in the meteorological forecast: cloud cover, irradiance variability, aerosol optical depth, and the timing of regime transitions. A probabilistic PV forecast that does not inherit and represent meteorological uncertainty faithfully will produce decision-relevant errors even if its point forecast is accurate. The growing emphasis on probabilistic extensions of solar power curves and on regime-aware forecasting reinforces the same conclusion: uncertainty information from meteorology is not an optional refinement but a core requirement for the next generation of PV forecasting systems.

The same meteorological dependency applies to other renewable energy forms. Wind power forecasting is fundamentally a meteorological problem: wind speed and direction forecasts from NWP or statistical downscaling constitute the primary input to turbine-level and farm-level power prediction, and the advective nature of wind makes the accuracy of the meteorological forecast the dominant control on forecast skill across horizons from minutes to days. The same applies to the link between hydrometeorological forecast and hydropower. The broader lesson is that as renewable energy's penetration rises, the accuracy of meteorological forecasting becomes a shared infrastructural requirement across PV, wind, and other sustainable resources, and improvements in atmospheric prediction translate directly into improved energy-system decision-making.

3. Data and Evaluation Methodology

3.1. Observational Data

In this study, we evaluate meteorological forecasts based on observations collected at three power generation sites, named ZJ, JX and QH (Figure 1). All three sites are located in the northern tropical region or midlatitudes; however, they differ substantially in elevation. Site ZJ and JX are about 2 m and 59 m above sea level, respectively, while site QH has an elevation of about 3104 m. Moreover, ZJ is a coastal site with marine climate influences, while the other two are located inland. Thus, they possess different climate conditions for validating the meteorological forecasts. The weather stations installed at these sites report the basic weather parameters at 15-min temporal resolution, including surface pressure, 2-m temperature, backplane temperature (for PV generation sites), 2-m relative humidity, 10-m wind direction and speed, direct radiation, scattered radiation and total (shortwave) radiation.

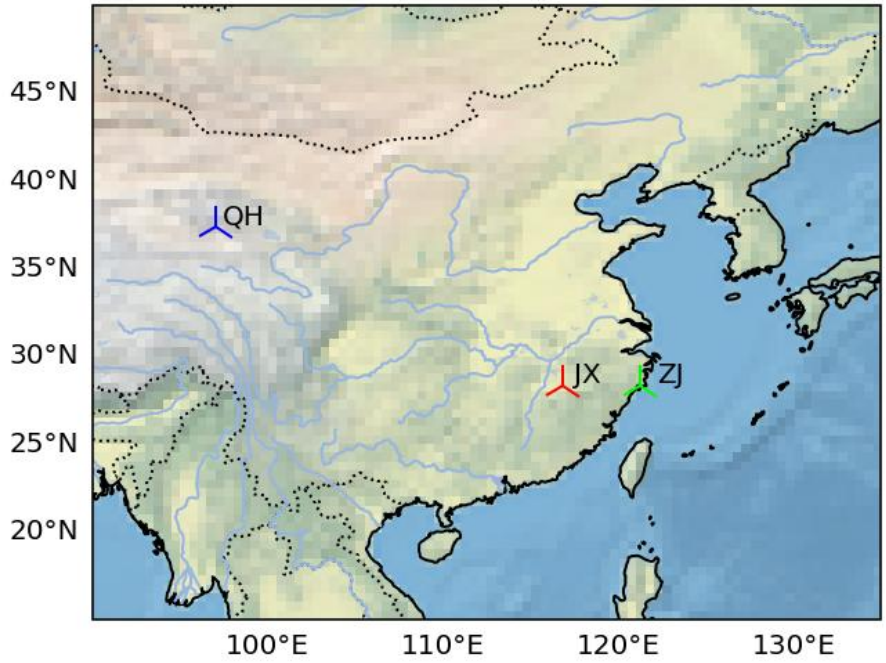


Figure 1. Geographic locations of the three PV sites (ZJ in green, JX in red and QH in blue) for model evaluation in this study. The elevations of the sites are 2 m (ZJ), 59 m (JX) and 3104 m (QH), respectively.

3.2. Meteorological Models

The first model (named GD model) to evaluate is a commercial weather forecast product acquired by Guodian Automation Co. Ltd., the owner of the three power generation sites in this study. The model is based on spatial and temporal downscaling products based on global operational weather model forecasts for specific site locations, with temporal resolution as high as 15-min and a 14-day lead time. While the details of the downscaling techniques are unknown, likely ensemble strategies have been implemented.

The Nanjing University of Information Science and Technology (NUIST) model is based on the global European Centre for Medium-range Weather Forecasts (ECMWF) integrated forecast system (IFS) with spatial resolution 0.25° latitude/longitude [16], which is one of the standard reference models for weather forecasters in the National Meteorological Center of the China Meteorological Administration and worldwide. The model forecasts are interpolated to the China region (60°—150° E, 10°S—70° N) with an increased resolution of 0.125° latitude/longitude. This model forecast has been operationally applied by the in-house weather forecasters of NUIST.

We also evaluate two global models with respect to radiative variables; one of them is the ECMWF-IFS high-resolution model. The model simulates at 9-km spatial resolution and 137 vertical levels and generates 15-day forecasts from every cycle of its 4D-variational data assimilation system [16]. The other model is the ICOsahedral Nonhydrostatic seamless model (ICON-seamless) from the German Weather Service (DWD; [17,18]). ICON-seamless is an integrated model with an atmospheric NWP component, land model, ocean-sea ice model, as well as an aerosol and reactive trace gas model. The NWP component has a spatial resolution of about 11 km and generates forecasts more than 7 days in lead.

https://doi.org/10.3390/meteorology5040044

3.3. Evaluation Methodology

There are two parts in our model evaluation: the first is for the 10-day forecasts of the major meteorological parameters, including surface pressure, 2-m air temperature, 2-m relative humidity, and 10-m wind direction and speed (Table 1). These are the essential parameters driving PV power forecast models and near-surface winds for wind power assessment and forecasting. The GD model forecasts are available at four initial times, which are 0000, 0800, 1200 and 1800 Beijing time (BJT, 8 h ahead of the universal coordinated time, UTC). The 0800 BJT forecast (i.e., from 0000 UTC) is important operationally because every morning that forecast is used to drive the PV model for ultrashort, short-term assessment and, of course, for outlook a week ahead as well. Thus, in the following, we mainly present evaluation results based on all the forecasts starting from 0800 BJT, while also comparing with the error metric statistics of all forecasts regardless of initial times.

Table 1. The forecast meteorological parameters from NWP models and those selected for evaluation in this study. For those not evaluated, downward shortwave is similar to the total radiation, while the cloud, rain and hydrometeorological parameters have incomplete data in the evaluation periods.

Parameter	Unit	Forecast Duration	Evaluated in This Study
Direct radiation	W m^{-2}	6 h	Yes
Scattered radiation	W m^{-2}	6 h	Yes
Total radiation	W m^{-2}	6 h	Yes
Downward shortwave	W m^{-2}	6 h	No
Surface pressure	hPa	10 days	Yes
2-m relative humidity	0–1 (100%)	10 days	Yes
2-m temperature	°C	10 days	Yes
10-m wind speed	m s^{-1}	10 days	Yes
10-m direction	0°–360°	10 days	Yes
Ice thickness	mm	10 days	No
Snow thickness	mm	10 days	No
15-min accumulated rain	mm	10 days	No
Total cloud cover	mm	10 days	No
Column cloud water	1–10	10 days	No

In the second part, we focus on ultrashort-term (6-h) forecasts of solar radiation with its three components (direct, scattered or diffuse and total; Table 1), which is the critical timescale for daily PV generation operations. While the GD model possesses 2-week forecasts of these radiation components, we only have access to the short-term forecasts from the ECMWF and ICON models and thus constrain the evaluation to the first 6 h. It should be noted that weather and climate models simulate the total direct and diffuse radiation reaching the Earth's surface. In other words, the direct outputs from the models are the global horizontal irradiance (GHI) and diffuse horizontal irradiance (DHI). In operation, solar panels are tilted and, in some systems, also have solar tracking according to the zenith angle of the Sun, such that the direct normal irradiance (DNI) to the panels is maximized. As a meteorology-based evaluation, our focus is GHI and DHI in this study and thus the results apply to both tracking and non-tracking systems. In fact, DHI is an important component in PV output for non-tracking systems and also in regions with frequent cloud cover.

Evaluation is based on standard error metrics common in model performance studies [19–21], which include

Mean bias (*MB*):

$$MB = \frac{1}{n}\sum_{i=1}^{n}(M_i - O_i), \quad (1)$$

Mean absolute error (*MAE*):

$$MAE = \frac{1}{n}\sum_{i=1}^{n}(|M_i - O_i|), \quad (2)$$

Mean absolute percentage error (*MAPE*):

$$MAPE = \frac{100\%}{n}\sum_{i=1}^{n}\left(\left|\frac{M_i - O_i}{O_i}\right|\right), \quad (3)$$

Root-mean-square error (*RMSE*):

$$RMSE = \sqrt{\frac{1}{n}\sum_{i=1}^{n}(M_i - O_i)^2}, \quad (4)$$

Index of agreement (*IOA*):

$$IOA = 1 - \frac{\sum_{i=1}^{n}(M_i - O_i)^2}{\sum_{i=1}^{n}(|M_i - \bar{O}| + |O_i - \bar{O}|)^2}, \quad (5)$$

Pearson correlation coefficient (*R*):

$$R = \frac{\sum_{i=1}^{n}((O_i - \bar{O})(M_i - \bar{M}))}{\sqrt{\sum_{i=1}^{n}(O_i - \bar{O})^2 \sum_{i=1}^{n}(M_i - \bar{M})^2}}, \quad (6)$$

In Equations (1) to (6), M_i and O_i are the model forecasts and observations, respectively, n is the number of samples (i.e., how many days of forecast in our evaluation periods), and overbar represents the mean. Among the metrics, IOA measures the relative model error from observations with respect to the average deviation of model forecasts and individual observations from the observed mean, which is close to 1.0 for a good match with observations. For the Pearson correlation coefficient, we apply it between the 240-h (10-day) forecast and observed time series.

Based on the available model forecast data, the evaluation periods for the three power generation sites are slightly different, which are January 2023—November 2024 for site ZJ, October 2024—August 2025 for site JX, and December 2024—August 2025 for site QH. While the periods for sites JX and QH are relatively short, they still cross the seasons from late autumn to early summer and can reveal quite thorough model performance at those locations. Moreover, tests have been conducted to reduce the evaluation period for site ZJ to 11 months (January–November 2024), which show that most error metrics have minimal changes (~1–2%), except for *MB* of variables such as surface pressure, relative humidity and wind direction that fluctuate largely. The innovations in our methodology, especially those relevant to PV operations, are highlighted in Table 2.

Table 2. Highlights of the methodology applied in this study.

Methodological Aspect	Highlight
Observations at the PV plants used	15-min observational data at the plants are used to evaluate the models.
Diverse evaluation sites	The three evaluation sites have very different elevations and climatology.
Comparison of major operational models plus a university model	Both global and regional models are evaluated for identifying site-specific strengths
Wide range of error metrics	The metrics can reveal different aspects of weaknesses in the models.
Two forecast timescales matched to PV operations	Both short-term (6 h) to mid-term (10 days) forecasts are evaluated for different operational needs.
Operationally relevant initialization time	Forecasts from the operationally critical initial time (0800 BJT) are especially evaluated.
Uncertainty characterization	Percentile ranges (25th–75th) are used to quantify spread in bias and absolute error.
Model-chain relevance	Evaluation targets the meteorological driver component of the PV power forecast chain.

4. Results

4.1. Ten-Day Forecasts of Meteorological Variables

First, the GD model has substantial biases in surface pressure at the QH site, as indicated by *MB*, *MAE*, *MAPE* and *RMSE* (Tables 3–6), indicating that the model may have issues simulating the pressure at high altitudes. The model's biases in surface temperature are also much larger than the NUIST model at the QH site. Also notable is that both the GD and NUIST models underestimate surface temperature at all three sites (Table 3), indicating a systematic issue in both models. Within the 10-day forecast period, the error metrics (*MB*, *MAE* and *RMSE*) possess clear diurnal variation and an increasing trend with forecast lead time (Figure 2). For bias and absolute error of temperature, the 25th and 75th percentiles among the samples indicate similar ranges of error from the two models, with that of the GD model slightly larger, implying the model fluctuates more in simulated temperature. Overall, the percentage changes in *MAE* (NUIST with respect to GD) at the three sites are ZJ (−6.7%/−6.8%), JX (1.1%/2.8%), QH (−51.9%/−52.6%) (first value is the average of all initialization times; second value for 0800 BJT initialization time), respectively. Both models have *IOA* values close to 1.0 in temperature (Figure 2 and Table 7), especially true at the ZJ site and the IOA values for surface humidity and wind direction are also higher at that site. These imply that the models can simulate the fluctuations of these variables around the observed mean at the coast better compared with the inland locations.

For surface relative humidity, performances of the two models do not differ much (Tables 3–6). However, the GD model does have a slightly higher Pearson correlation coefficient R for the 10-day forecast period across the three sites (Table 8), which also applies to surface temperature. Similar to surface temperature, the error metrics of humidity have diurnal variations, while the models' *IOA* slightly decreases from about 0.9 across the 10-day forecast period (Figure 3). The 25th and 75th percentile values of the bias and absolute error also have a large range, which is similar for both models.

Table 3. Mean bias (*MB*) averaged over a 10-day forecast period for the GD and NUIST models in surface pressure (Psfc), 2-m temperature (T2m), 2-m relative humidity (RH2m), 10-m wind direction (WD10m) and speed (WS10m) at the three evaluation sites (ZJ, JX and QH) for all initial times and only those initialized at 0800 Beijing time (BJT). For each site, the model with the lowest *MB* magnitude is in bold.

		Psfc (hPa)	T2m (°C)	RH2m (%)	WD10m (deg.)	WS10m (m/s)
All initial times						
NUIST	ZJ	**−1.554**	**−1.0493**	**−0.146**	−9.349	**2.546**
	JX	**−1.206**	**−0.247**	−11.900	−5.236	1.673
	QH	**2.986**	**−0.409**	**−2.370**	−11.790	**−0.663**
GD	ZJ	−6.858	−1.463	1.317	**−5.881**	3.0385
	JX	−6.363	−0.569	**−10.800**	**−0.0840**	1.489
	QH	−24.201	−4.235	7.220	**8.677**	**−0.155**
0800 BJT initial time						
NUIST	ZJ	**−1.584**	**−1.0334**	**−0.0616**	−8.878	**2.534**
	JX	**−1.239**	**−0.277**	−12.000	−5.124	1.675
	QH	**2.942**	**−0.409**	**−2.370**	−11.609	−0.672
GD	ZJ	−6.857	−1.457	1.323	**−5.922**	3.0622
	JX	−6.422	−0.558	**−10.800**	**−0.120**	**1.494**
	QH	−24.465	−4.247	7.0700	**8.876**	**−0.148**

Table 4. As in Table 3, except for mean absolute error (*MAE*). For each site, the model with the lowest *MAE* is in bold.

		Psfc (hPa)	T2m (°C)	RH2m (%)	WD10m (deg.)	WS10m (m/s)
All initial times						
NUIST	ZJ	**5.953**	**1.964**	9.568	85.755	**2.574**
	JX	**1.816**	1.913	14.445	107.121	1.850
	QH	**3.0462**	**2.240**	**10.015**	80.889	1.621
GD	ZJ	10.00117	2.105	**9.402**	**75.923**	3.0455
	JX	6.307	**1.892**	**12.648**	**89.873**	**1.660**
	QH	23.706	4.656	12.620	**68.352**	**1.534**
0800 BJT initial time						
NUIST	ZJ	**6.00675**	**1.962**	9.520	85.456	**2.562**
	JX	**1.850**	2.120	13.710	105.338	1.791
	QH	**3.0224**	**2.273**	**9.710**	78.417	1.634
GD	ZJ	10.0529	2.106	**9.394**	**75.884**	3.0691
	JX	6.381	**2.0622**	**11.900**	**88.449**	**1.617**
	QH	24.119	4.797	12.270	**66.470**	**1.537**

Table 5. As in Table 3, except for mean absolute percentage error (*MAPE*). For each site, the model with the lowest *MAPE* is in bold.

		Psfc (%)	T2m (%)	RH2m (%)	WS10m (%)
All initial times					
NUIST	ZJ	**0.26**	**0.63**	**12.36**	**268.67**
	JX	**0.18**	0.67	17.94	164.82
	QH	**0.45**	**0.78**	**33.24**	**62.05**
GD	ZJ	0.83	0.71	13.94	304.53
	JX	0.63	**0.63**	**15.70**	**142.55**
	QH	3.43	1.57	53.64	67.06
0800 BJT initial time					
NUIST	ZJ	**0.26**	**0.63**	**12.37**	**264.74**
	JX	**0.18**	0.67	18.03	165.97
	QH	**0.44**	**0.78**	**33.06**	**62.04**
GD	ZJ	0.83	0.71	13.86	308.25
	JX	0.64	**0.63**	**15.57**	**143.75**
	QH	3.47	1.58	53.35	66.90

Table 6. As in Table 3, except for root-mean-square error (*RMSE*). For each site, the model with the lowest *RMSE* is in bold.

		Psfc (hPa)	T2m (°C)	RH2m (%)	WD10m (deg.)	WS10m (m/s)
All initial times						
NUIST	ZJ	46.712	**2.611**	12.566	98.722	**3.0352**
	JX	**1.964**	2.320	16.100	**87.613**	1.991
	QH	**3.286**	**2.573**	**11.800**	81.321	1.958
GD	ZJ	**40.676**	2.754	**12.129**	**90.660**	3.414
	JX	6.463	**2.199**	**14.400**	89.330	**1.751**
	QH	24.270	4.746	13.400	**79.345**	**1.786**
0800 BJT initial time						
NUIST	ZJ	46.839	**2.607**	12.505	98.468	**3.0211**
	JX	**1.992**	2.316	16.100	**87.580**	1.991
	QH	**3.254**	**2.565**	**11.800**	81.322	1.947

GD	ZJ	**40.986**	2.750	**12.0994**	**90.616**	3.436
	JX	6.520	**2.170**	**14.200**	88.994	**1.756**
	QH	24.553	4.719	13.400	**79.613**	**1.764**

Table 7. As in Table 3 except for index of agreement (*IOA*). For each site, the model with the highest *IOA* is in bold.

		Psfc (hPa)	T2m (°C)	RH2m (%)	WD10m (deg.)	WS10m (m/s)
All initial times						
NUIST	ZJ	0.125	**0.973**	**0.822**	**0.754**	**0.307**
	JX	**0.638**	0.787	0.621	**0.398**	0.344
	QH	**0.444**	**0.846**	**0.681**	**0.555**	**0.496**
GD	ZJ	**0.166**	0.969	0.816	0.721	0.275
	JX	0.284	**0.806**	**0.655**	0.375	**0.371**
	QH	0.0838	0.687	0.591	0.526	0.443
0800 BJT initial time						
NUIST	ZJ	0.124	**0.973**	**0.826**	**0.753**	**0.311**
	JX	**0.634**	0.796	0.613	**0.396**	0.345
	QH	**0.453**	**0.850**	**0.681**	**0.555**	**0.493**
GD	ZJ	**0.165**	0.969	0.817	0.722	0.273
	JX	0.282	**0.816**	**0.647**	0.375	**0.367**
	QH	0.0847	0.696	0.599	0.523	0.443

Table 8. Pearson correlation coefficient (*R*) between observations and forecasts in 10-day periods for the GD and NUIST models, averaged over all initial times and only those initialized at 0800 Beijing time (BJT). For each site, the model with the highest R is in bold.

		T2m (°C)	RH2m (%)	WD10m (deg.)	WS10m (m/s)
All initial times					
NUIST	ZJ	0.958	0.728	**0.661**	**0.354**
	JX	0.828	0.719	**0.0313**	0.130
	QH	0.879	0.735	0.285	0.296
GD	ZJ	**0.960**	**0.758**	0.543	0.339
	JX	**0.868**	**0.784**	0.0300	**0.210**
	QH	**0.899**	**0.752**	**0.349**	**0.339**
0800 BJT initial time					
NUIST	ZJ	0.958	0.734	**0.667**	0.360
	JX	0.852	0.723	0.0231	0.138
	QH	0.903	0.739	0.283	0.291
GD	ZJ	**0.961**	**0.760**	0.545	0.333
	JX	**0.896**	**0.788**	**0.0304**	**0.186**
	QH	**0.925**	**0.761**	**0.344**	**0.343**

Compared with the thermodynamic variables, it is expected that simulated biases in the dynamic variables of wind direction and speed would be larger, especially for the evaluation sites here with strong coastal (land-sea breeze) and topographic (high altitude) influences. The error metrics of *MB*, *MAE* and *RMSE* indicate slightly better performance in simulating 10-m wind direction by the GD model (Tables 3–6). However, the NUIST model excels in having higher *IOA* across the three sites (Table 7), indicating that it agrees better with the observed wind direction fluctuations around the mean. Although wind direction may not have a direct impact on wind energy production, the large *MAE* and *RMSE* of simulated wind direction, together with very large ranges between the 25th and

75th percentiles (Figure 4), indicate that the models possess large uncertainties in simulating the regional circulation systems. Both models simulate a higher Pearson correlation coefficient *R* at the coastal ZJ site versus the other two inland sites (Table 8), which may be due to stronger forcing of land-sea breeze controlling the wind direction.

In terms of wind speed, all the error metrics (*MB*, *MAE*, *RMSE*, *IOA* and *R*) indicate that the NUIST model performs better at the coastal site ZJ (Tables 3–8 and Figure 5), while the GD model excels at the two inland sites with only a small margin. For example, the percentage changes in *MAE* (NUIST with respect to GD) at the three sites are ZJ (−15.5%/−16.5%), JX (11.4%/10.8%), QH (5.7%/6.3%) (all initialization times/0800 BJT initialization time), respectively. Wind speed is also a highly intermittent variable and thus such nature is also manifested in the error metrics time series (Figure 5), and the large associated 25th to 75th percentile range.

One additional remark is that all the results discussed so far are consistent between evaluation for the forecast initialized at 0800 BJT and that average over all initialization times.

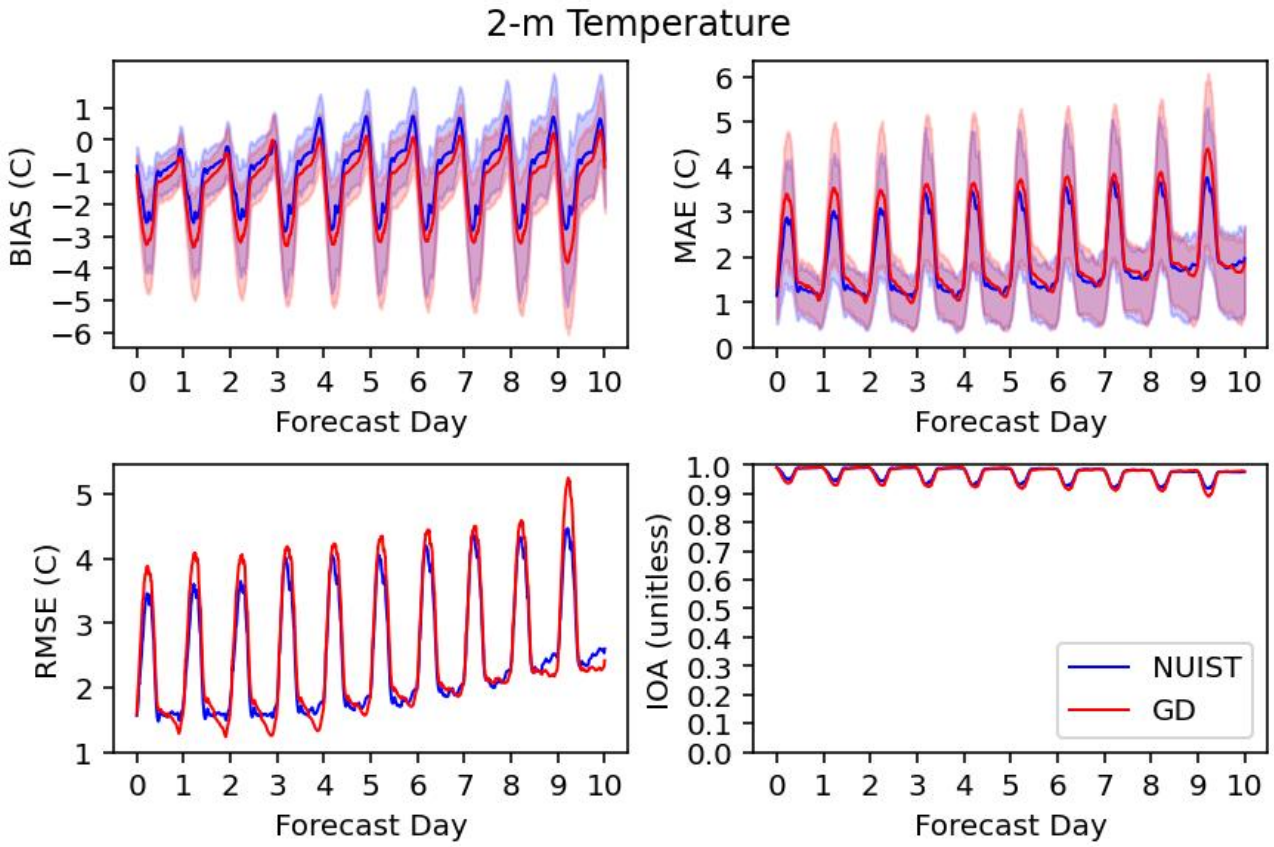


Figure 2. *MB*, *MAE*, *RMSE* and *IOA* (lines) in the forecast initialized at 0800 BJT of 2-m temperature from the GD and NUIST models based on 15-min time series. For bias and absolute error, the 25% and 75% percentiles in all forecast samples are shown as shaded areas with corresponding colors.

https://doi.org/10.3390/meteorology5040044

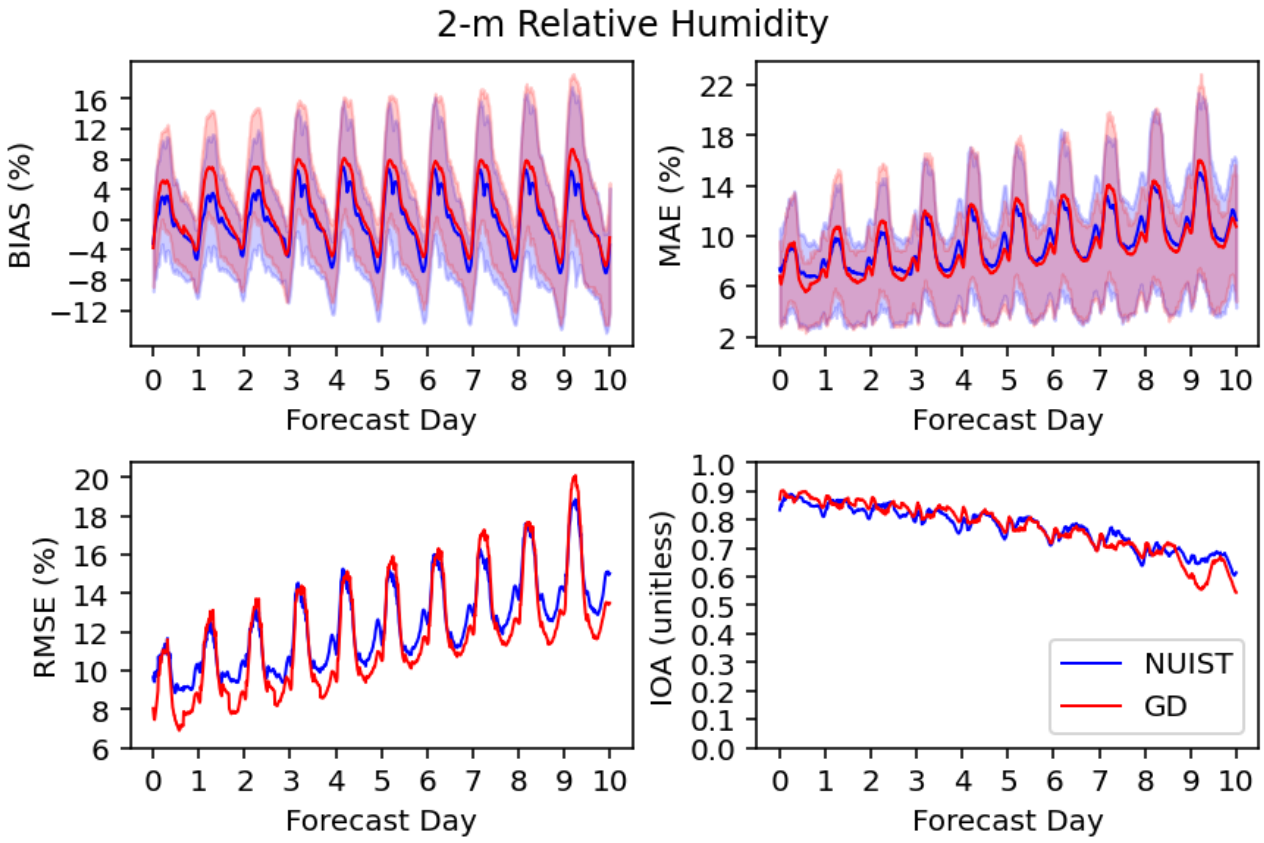


Figure 3. As in Figure 2, except for 2-m relative humidity.

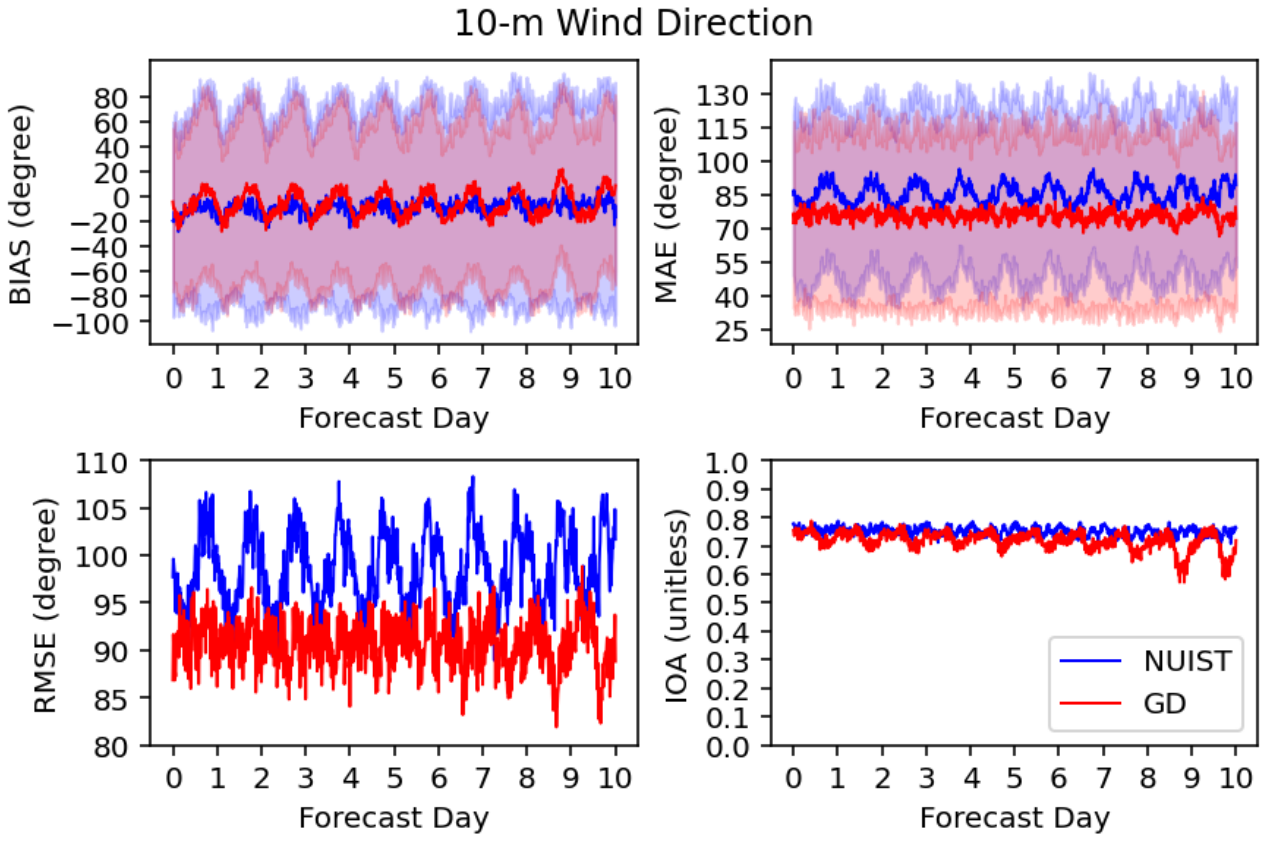


Figure 4. As in Figure 2, except for 10-m wind direction.

https://doi.org/10.3390/meteorology5040044

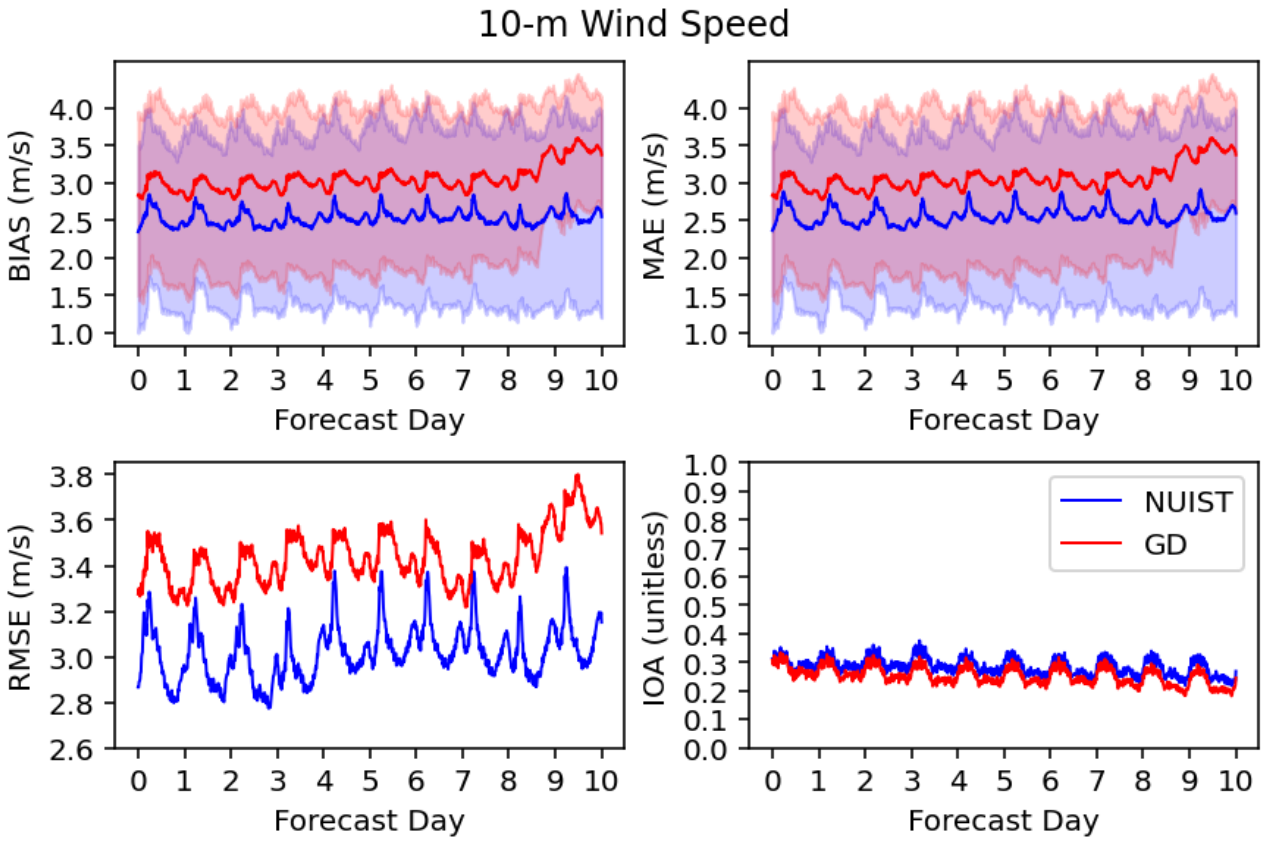


Figure 5. As in Figure 2, except for 10-m wind speed.

4.2. Ultrashort-Term Forecasts of Solar Radiation

In the 6-h forecasts of the radiation variable (direct, scattered, total), there are some general features identified. First, the *MB*, *MAE* and *RMSE* of direct radiation forecasts at the QH site are much lower than those at the two other sites (Tables 9–12). While the exact reason is unclear, it may be due to the strong solar radiation received at an altitude above 3 km and thus the forecast skill of direct radiation is generally higher than that over plain areas. Secondly, all three models overestimate direct radiation at the low-altitude sites (ZJ and JX), while underestimating the scattered radiation (Table 9). Eventually, the models overestimate total shortwave radiation at ZJ but underestimate it at JX (Table 9).

Comparing the three models, it is clear that the EC-IFS and ICON models outperform the GD model for direct radiation, at least at the ZJ site (Figure 6). For scattered radiation, the ranking of the models varies for different error metrics (Figure 7 and Tables 9–12). In particular, the GD model is skillful at simulating scattered radiation at the high-altitude QH site. If focusing on the *MAE*, the ICON model certainly stands out as it has the smallest *MAE* (averaged over all initialization times) across the three sites (Table 10). The model also has consistently low *MB*, *RMSE* and high *IOA* (Figure 8, Table 13). Quantitatively, the percentage changes in *MAE* (ICON with respect to GD) at the three sites are ZJ (−26.8%/−6.0%), JX (−0.4%/1.5%), QH (−1.35%/−1.1%) (all initialization times/0800 BJT initialization time), respectively. However, for these three components of radiation, it can also be seen that the ranges of bias and absolute error across our samples are large (Figures 6–8).

Similar to the meteorological variables, these major evaluation results for the radiation components are about the same for forecasts initialized at 0800 BJT and those averaged over all initialization times; the former is certainly the most important forecast cycle, as it includes the peak radiative power of a day.

Table 9. Mean bias (*MB*) averaged over 6-h forecast period for the GD, EF-IFS and ICON models in direct radiation, diffuse (scattered) radiation, and total radiation at the three evaluation sites (ZJ, JX and QH) for all initial times and only those initialized at 0800 Beijing time (BJT). For each site, the model with the lowest *MB* magnitude is in bold.

		Direct Radiation	Diffuse (Scattered)	Total Shortwave
All initial times				
EC-IFS	ZJ	83.528	**−57.847**	25.827
	JX	122.392	−108.949	−23.648
	QH	**2.889**	92.873	−26.0409
ICON	ZJ	**66.222**	−64.0676	**13.822**
	JX	**112.511**	**−108.430**	−33.0106
	QH	15.831	83.174	−22.797
GD	ZJ	174.0137	−154.812	37.229
	JX	162.161	−145.832	**−20.974**
	QH	92.167	**13.0113**	**−17.0565**
0800 BJT initial time				
EC-IFS	ZJ	240.494	**−176.776**	64.0346
	JX	277.720	**−258.494**	−53.716
	QH	**−8.575**	157.888	−63.192
ICON	ZJ	**199.857**	−200.740	**26.792**
	JX	**256.692**	−258.0370	−74.287
	QH	14.577	142.716	−55.212
GD	ZJ	355.442	−315.509	75.944
	JX	368.0526	−339.773	**−45.163**
	QH	151.842	**21.892**	**−39.936**

Table 10. As in Table 9, except for mean absolute error (*MAE*). For each site, the model with the lowest *MAE* is in bold.

		Direct Radiation	Diffuse (Scattered)	Total Shortwave
All initial times				
EC-IFS	ZJ	**87.175**	90.0163	54.574
	JX	122.689	131.136	70.699
	QH	**53.365**	92.880	93.495
ICON	ZJ	99.242	**88.214**	**49.958**
	JX	**112.986**	**126.751**	**68.755**
	QH	66.877	83.192	**80.430**
GD	ZJ	210.855	161.0265	68.213
	JX	162.162	147.546	69.0537
	QH	94.309	**13.0921**	81.659
0800 BJT initial time				
EC-IFS	ZJ	**250.535**	**253.313**	143.930
	JX	278.472	299.562	147.344
	QH	**82.844**	157.889	136.686
ICON	ZJ	278.520	254.990	**130.157**
	JX	**257.886**	**290.994**	144.245
	QH	107.246	142.717	**129.0979**
GD	ZJ	428.904	327.720	138.448
	JX	368.0526	340.939	**142.0846**
	QH	154.695	**22.0086**	130.515

Table 11. As in Table 9, except for mean absolute percentage error (*MAPE*). For each site, the model with the lowest *MAPE* is in bold. The *MAPE* for diffuse radiation at the site QH fluctuates substantially due to the occasional low observational value, leading to an exceptionally high *MAPE* that is treated as invalid.

		Direct Radiation (%)	Diffuse (Scattered) (%)	Total Shortwave (%)
All initial times				
EC-IFS	ZJ	91.79	70.40	69.77
	JX	460.52	50.81	59.82
	QH	**43.30**	–	41.71
ICON	ZJ	**87.24**	**66.66**	63.04
	JX	**439.20**	**48.62**	**58.31**
	QH	46.44	–	**40.54**
GD	ZJ	108.38	71.42	**58.74**
	JX	493.03	58.86	63.78
	QH	72.60	–	43.89
0800 BJT initial time				
EC-IFS	ZJ	84.07	63.56	66.49
	JX	464.11	64.88	37.74
	QH	**35.92**	–	36.26
ICON	ZJ	**74.20**	**55.17**	**50.65**
	JX	**447.11**	**60.98**	**35.28**
	QH	41.04	–	**34.86**
GD	ZJ	120.04	74.42	63.78
	JX	495.33	71.93	37.17
	QH	69.93	–	38.73

Table 12. As in Table 9, except for root-mean-square error (*RMSE*). For each site, the model with the lowest *RMSE* is in bold.

		Direct Radiation	Diffuse (Scattered)	Total Shortwave
All initial times				
EC-IFS	ZJ	**178.811**	**185.214**	112.855
	JX	162.637	176.381	100.141
	QH	**77.116**	112.695	111.161
ICON	ZJ	220.556	191.754	**111.795**
	JX	**156.824**	**172.748**	99.657
	QH	93.317	107.348	110.220
GD	ZJ	337.125	290.259	136.522
	JX	187.531	193.593	**98.291**
	QH	122.469	**17.537**	**109.482**
0800 BJT initial time				
EC-IFS	ZJ	**317.501**	**328.130**	196.739
	JX	349.961	380.766	187.689
	QH	**115.984**	185.893	171.307
ICON	ZJ	386.471	343.595	**190.215**
	JX	**339.583**	**374.693**	189.455
	QH	147.454	180.0759	168.340
GD	ZJ	481.315	414.482	194.916
	JX	405.898	419.482	**181.434**
	QH	197.600	**30.121**	**167.315**

Table 13. As in Table 9, except for the index of agreement (*IOA*). For each site, the model with the highest *IOA* is in bold.

		Direct Radiation	Diffuse (Scattered)	Total Shortwave
All initial times				
EC-IFS	ZJ	0.0850	**0.751**	**0.952**
	JX	0.119	0.707	0.696
	QH	**0.888**	0.119	0.893
ICON	ZJ	0.288	0.652	0.947
	JX	**0.121**	**0.721**	**0.704**
	QH	0.875	0.113	**0.899**
GD	ZJ	**0.307**	0.511	0.945
	JX	0.0990	0.617	0.637
	QH	0.815	**0.590**	0.897
0800 BJT initial time				
EC-IFS	ZJ	0.0887	**0.518**	0.862
	JX	0.238	0.498	0.889
	QH	**0.927**	0.0991	0.924
ICON	ZJ	0.251	0.502	**0.872**
	JX	**0.240**	0.518	**0.892**
	QH	0.897	0.0883	**0.928**
GD	ZJ	**0.266**	0.503	0.851
	JX	0.198	**0.528**	0.891
	QH	0.833	**0.538**	0.927

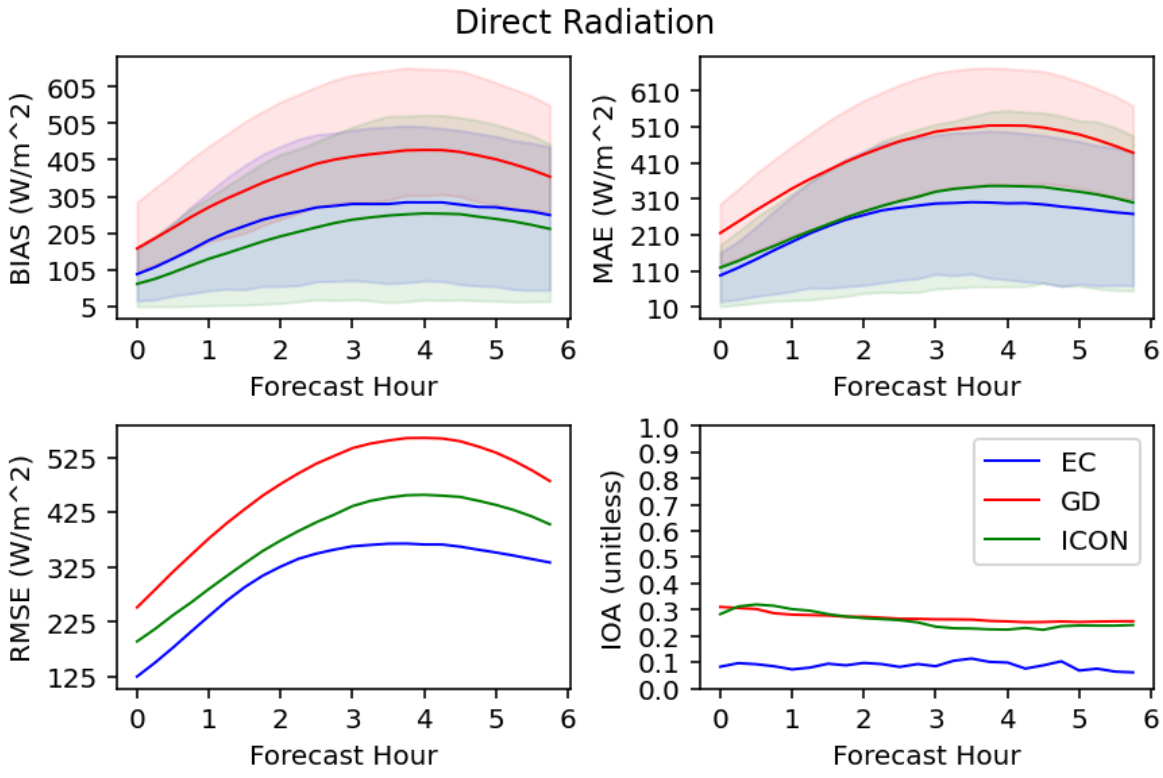


Figure 6. *MB*, *MAE*, *RMSE* and *IOA* (lines) in forecasts initialized at 0800 BJT of direct radiation from the EC, GD and ICON models based on 15-min time series. For bias and absolute error, the 25% and 75% percentiles in all forecast samples are shown as shaded areas with corresponding colors.

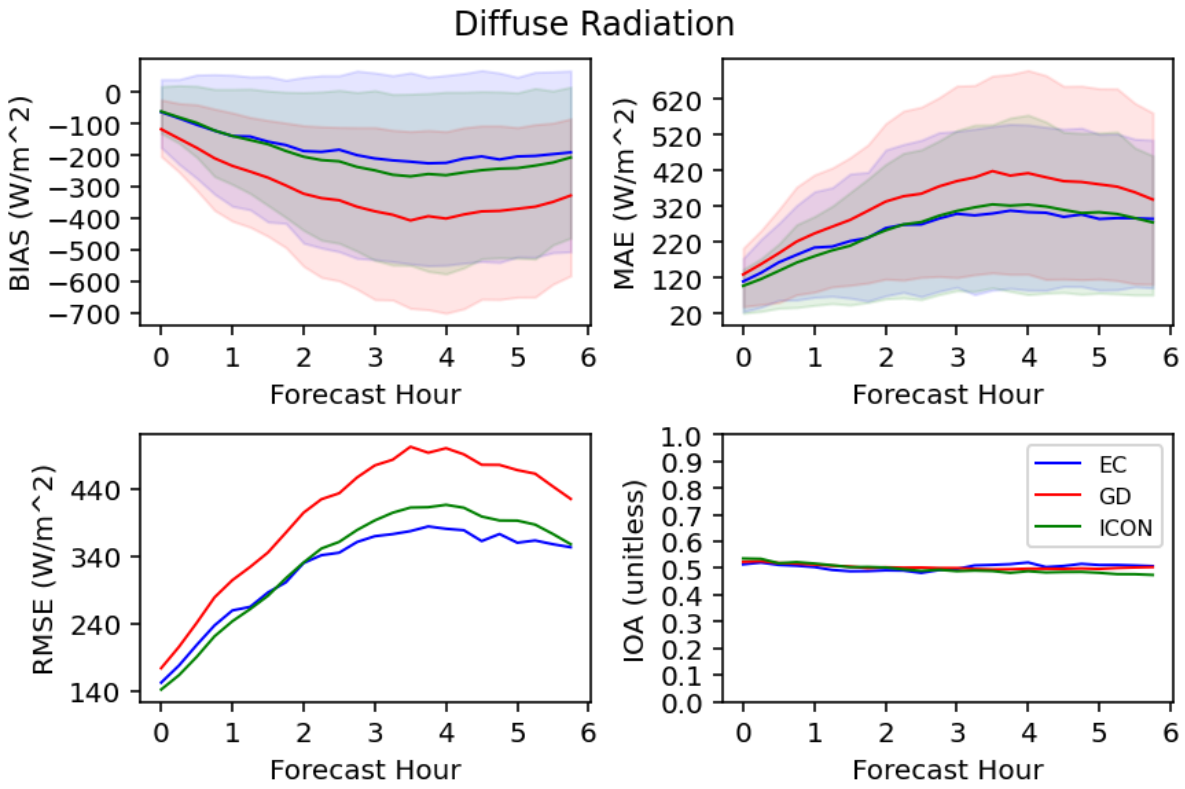


Figure 7. As in Figure 6, except for diffuse radiation.

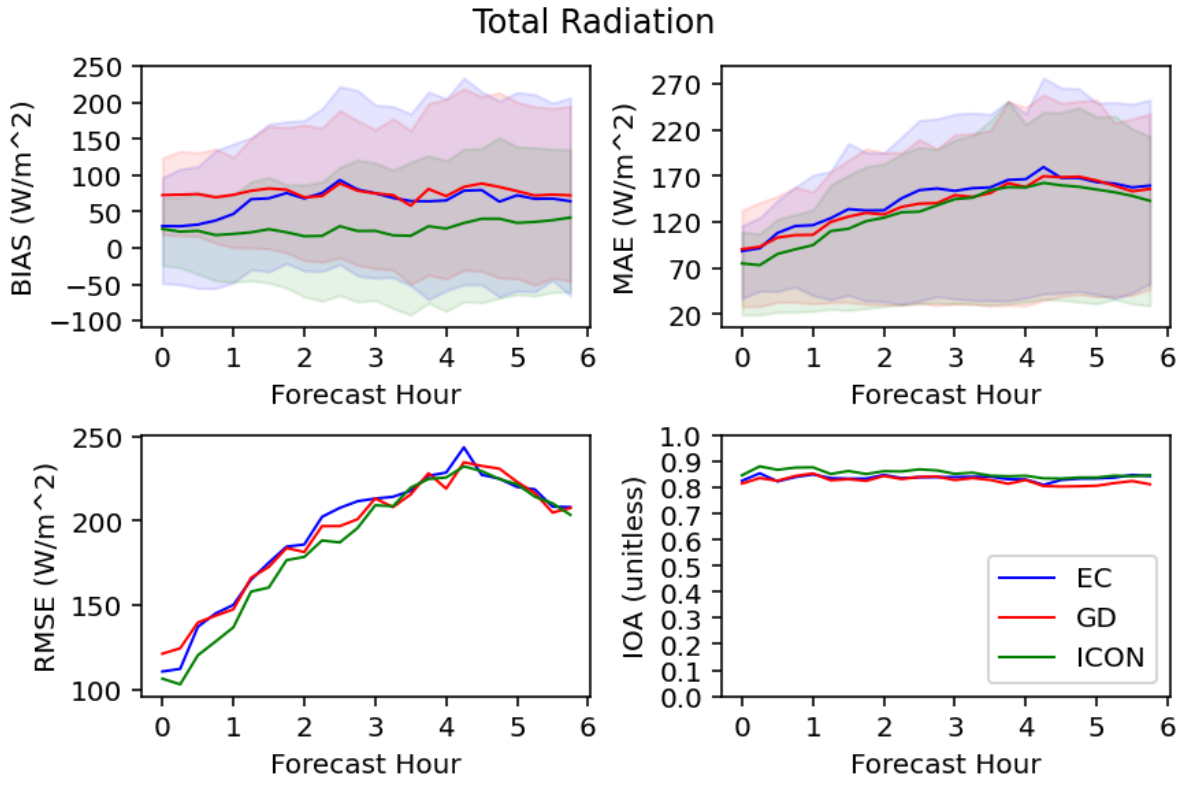


Figure 8. As in Figure 6, except for total radiation.

https://doi.org/10.3390/meteorology5040044

5. Discussion and Conclusions

5.1. Discussion

There are certain limitations in this study. First is the limited number of weather stations evaluated, although they are diverse geographically and climatologically. A denser network of stations can reveal the regional characteristics and inter-regional differences in model performance better. Secondly, the weather station data applied here have only gone through basic quality control but not a rigorous QA/QC process, as for the stations operated by the China Meteorological Administration (CMA). Work is undergoing to evaluate the observations at the PV sites based on CMA data in the vicinity, such that future comparison with model forecasts will be more robust. Thirdly, the evaluation periods for the three stations are not homogeneous, with the shortest being less than one year. Future evaluations will include longer and homogeneous periods of data for all stations such that seasonal evaluation is also feasible.

Our results indicate that biases in wind speed and wind direction forecasts are the largest among the variables. There have been arguments that whether wind speed has impacts to PV power forecasting or is negligible. By examining different modeling pathways for PV power forecasting (e.g., [6,14]), it becomes clear that wind speed may not be the foundation as for irradiance; however, it is a physically meaningful auxiliary input that becomes operationally relevant in model-chain architectures through the thermal conversion step, and its uncertainty contributes to the overall probabilistic power forecast. Moreover, the weight of wind speed is also regime-dependent: Wind speed forecasts matter more for power prediction under low-irradiance or high-temperature conditions when the thermal sensitivity of the module is higher. Overall, the added value of wind speed information to power prediction depends on the link in the model chain, operating conditions and forecast product (deterministic vs. probabilistic).

As mentioned in the introduction, power forecasting at various timescales is important for operational renewable energy production. Currently, the renewable energy sector at Guodian Nanjing Automation Co. Ltd. applies a deep learning-based PV power forecast model. The model is efficient in terms of computational requirements. For each site and input of two years of observations and meteorological forecasts, model training can be completed within minutes. Thus, many meteorological models and PV sites can be experimented with efficiently. In the past, meteorological forecasts from the GD model have been used as a training dataset for the PV power forecast model, which has learned the forecast error characteristics of GD. Our evaluation study has shown that other global or regional meteorological models may perform better than GD in selected physical parameters. Thus, we are in the process of retraining the PV power forecast model with the meteorological models evaluated in this study, which aims to confirm to what degree improved meteorological forecasts lead to improvements in PV power forecasts. After we examine these impacts on power forecasts, a selected ensemble forecast strategy will be tested and implemented for the current operational procedure. The selected ensemble system not only consists of optimized models for individual meteorological inputs but also an optimized combination of models for different timescales of concern in PV assessment.

Dynamical models for predicting PV resources have been developed, such as the WRF-Solar model (e.g., [22,23]). While these models, with improved radiative process representation compared with conventional atmospheric models, can generate promising predictions of PV power, in most operational scenarios they are too computationally heavy. For example, the PV power forecast initialized at 0800 BJT (0000 UTC) is the most critical to commence operational planning every day, which often starts two hours before 0800 BJT. Thus, additional computational time for a dynamical model forecast to complete

would cause a delay in operational planning. Comparatively, a computationally efficient strategy that applies optimized meteorological inputs and a suitably trained PV model seems to be the most cost-effective framework for the industry.

Nonetheless, the global and even the regional NWP models often have low skill in forecasting short-term variability in cloud cover, which in turn affects the PV estimation accuracy. This can clearly be seen in our evaluation of the 6-h DNI, DHI and GHI forecasts. These scenarios are often associated with abrupt changes in weather, such as during thunderstorms and tropical cyclone landfall. It is also for these weather systems that spatially dislocated forecast errors are common, which affect the PV resource estimate in the power plant network. Thus, one of the major tasks in our future work will be the incorporation of real-time, in-situ observations of cloud cover and solar radiation, such that a true data fusion of ultrashort-term solar radiation forecasts, medium-term model-based meteorological simulations, statistical/deep-learning PV power model and observations-based adjustment (e.g., identification of high-impact weather) can be designed for optimizing short- and ultrashort-term PV forecasts.

5.2. Conclusions

This study evaluated the performance of four meteorological models (GD, NUIST, ECMWF-IFS, and ICON) in simulating key PV-relevant variables at three diverse power generation sites in China. The main conclusions are as follows.

(1) For 10-day forecasts, the NUIST model significantly outperforms the GD model in 2-m temperature at the high-altitude QH site, with mean absolute error (*MAE*) reductions of approximately 52% (averaged over all initialization times and the 0800 BJT cycle). However, both models show a systematic cold bias at all three sites. In terms of 10-m wind speed, the NUIST model performs better at the coastal ZJ site (*MAE* reduction of ~16%), while the GD model holds a slight edge at the inland JX and QH sites (*MAE* increases of 11% and 6% for NUIST, respectively). Wind direction remains challenging for both models, as evidenced by large *MAE*/*RMSE* values and wide interquartile ranges, though the NUIST model achieves a higher index of agreement (*IOA*) at all sites.

(2) For ultrashort-term (6-h) solar radiation forecasts, the ICON model consistently demonstrates the best overall performance. Compared to the GD model, ICON reduces *MAE* for total shortwave radiation by 26.8% at ZJ, with modest improvements at JX and QH. All models overestimate direct radiation at low-altitude sites (ZJ, JX) and underestimate scattered radiation. The high-altitude QH site exhibits much lower error metrics for direct radiation, likely due to stronger and less variable incoming solar radiation.

(3) Regardless of model or variable, error metrics increase with forecast lead time and exhibit clear diurnal variations. The 25th–75th percentile ranges of bias and absolute error are notably large for wind and humidity, reflecting the inherent intermittency and stochastic nature of these variables. The coastal ZJ site generally yields higher *IOA* and correlation coefficients than inland sites, suggesting that stronger mesoscale forcing (e.g., land-sea breeze) improves model consistency.

Author Contributions: Conceptualization, K.K.W.C., Z.F., L.W., X.X. and Y.Y.; methodology, Y.L., Y.X., K.K.W.C., Z.D., Z.F. and X.X.; software, Y.L., Y.X., K.K.W.C., Z.D., Z.F. and L.W.; validation, Y.L., Y.X., K.K.W.C., Z.D. and Z.F.; formal analysis, Y.L., Y.X., K.K.W.C., Z.D. and Z.F.; investigation, Y.L., Y.X., K.K.W.C., Z.D. and Z.F.; resources, Y.L., Y.X., K.K.W.C., Z.F., L.W. X.X., L.H. and B.X.; data curation, Y.L., Y.X., K.K.W.C., Z.D., Z.F. and L.W.; writing—original draft preparation, Y.L., Y.X., K.K.W.C. and Z.D.; writing—review and editing, Y.L., Y.X., K.K.W.C., Z.D., Z.F., L.W., X.X., L.H., B.X. and Y.Y.; visualization, K.K.W.C., Z.D. and Z.F.; supervision, K.K.W.C., L.W., L.H., B.X. and Y.Y.; project administration, K.K.W.C., X.X., L.H., B.X. and Y.Y.; funding

acquisition, K.K.W.C., X.X., L.H., B.X. and Y.Y. All authors have read and agreed to the published version of the manuscript.

Funding: This research is supported by the Guodian Nanjing Automation Co., Ltd., Nanjing, China.

Data Availability Statement: Model data (ECMWF-IFS and ICON) are available publicly at https://open-meteo.com/ (last accessed 13 October 2026). The NUIST model data and station observations were obtained from NUIST and Guodian Nanjing Automation Co., Ltd., respectively, and are available from the authors with permission from the two parties.

Acknowledgments: This research is supported by a collaborative project between Guodian Automation Co., Ltd. and the Nanjing University of Information Science and Technology (NUIST). KKWC acknowledges support from the Startup Foundation for Introducing Talent from NUIST. The authors are grateful to the two anonymous reviewers for providing insightful and constructive comments for us to improve the manuscript.

Conflicts of Interest: Authors Ying Liu, Yunfei Xu, Lei Huang and Bitao Xiao are employed by the company Guodian Nanjing Automation Co., Ltd., Nanjing, China. The funder had no role in the design of the study; in the collection, analyses, or interpretation of data; in the writing of the manuscript; or in the decision to publish the results.

Abbreviations

The following abbreviations are used in this manuscript:

BJT	Beijing time
DHI	Diffuse horizontal irradiance
DNI	Direct normal irradiance
DWD ICON	Deutscher Wetterdienst ICOsahedral Nonhydrostatic model
ECMWF-IFS	European Centre for Medium-range Weather Forecast-Integrated Forecast System
GD	Guodian
GHI	Global horizonal irradiance
IOA	Index of agreement
JX	Jiangxi
MAE	Mean absolute error
MAPE	Mean absolute percentage error
MB	Mean bias
NWP	Numerical weather prediction
NUIST	Nanjing University of Information Science and Technology
PV	Photovoltaic
QH	Qinghai
RMSE	Root-mean-square error
UTC	Coordinated universal time
ZJ	Zhejiang

References

1. Olabi, A.; Abdelkareem, M. Renewable energy and climate change. *Renew. Sustain. Energy Rev.* **2022**, *158*, 112111. https://doi.org/10.1016/J.RSER.2022.112111.
2. Gernaat, D.; de Boer, H.; Daioglou, V.; Yalew, S.; Müller, C.; van Vuuren, D. Climate change impacts on renewable energy supply. *Nat. Clim. Change* **2021**, *11*, 119–125. https://doi.org/10.1038/s41558-020-00949-9.
3. Meucci, A.; Grossmann-Matheson, G.; Su, C.-H.; Hally, B.; Hernaman, V.; Machado, D.A.; Tamizi, A.; Young, I.R. Resilience of offshore wind resources in Australia under climate change using CMIP6 CORDEX projections. *Energy Clim. Change* **2026**, *7*, 100236. https://doi.org/10.1016/J.EGYCC.2026.100236.
4. de Freitas, N.C.A.; Silva, M.P.d.S.; Sakamoto, M.S. Wind speed forecasting: A review. *Int. J. Eng. Res. Appl.* **2018**, *8*, 4–9.

5. Mayer, M.; Gróf, G. Extensive comparison of physical models for photovoltaic power forecasting. *Appl. Energy* **2021**, *283*, 116239. https://doi.org/10.1016/J.APENERGY.2020.116239.
6. Yang, D.; Xia, X.; Mayer, M. A tutorial review of the solar power curve: Regressions, model chains, and their hybridization and probabilistic extensions. *Adv. Atmos. Sci.* **2024**, *41*, 1023–1067. https://doi.org/10.1007/s00376-024-3229-4.
7. van Duinen, B.; van der Most, L.; Baatsen, M.; van der Wiel, K. Meteorological drivers of co-occurring renewable energy droughts in Europe. *Renew. Sustain. Energy Rev.* **2025**, *223*, 115993. https://doi.org/10.1016/J.RSER.2025.115993.
8. Huang, J.; Yuan, C.; Boland, J.; Guo, S.; Liu, W. One-step ahead short-term hourly global solar radiation forecasting with a dynamical system based on classification of days. *Renew. Energy* **2024**, *237*, 121639. https://doi.org/10.1016/J.RENENE.2024.121639.
9. Belmahdi, B.; Bouardi, A. Short-term solar radiation forecasting using machine learning models under different sky conditions: Evaluations and comparisons. *Env. Sci. Pollut. Res.* **2024**, *31*, 966–981. https://doi.org/10.1007/s11356-023-31246-5.
10. Zeng, Z.; Wu, H.; Liu, Z.; Zhao, L.; Liang, Z.; Liang, Z.; Wang, Y. Enhancing short-term wind speed prediction capability of numerical weather prediction through machine learning methods, *J. Geophys. Res. Atmos.* **2024**, *129*, e2024JD041822. https://doi.org/10.1029/2024JD041822.
11. Klousakou, E.; Chalakatevaki, M.; Dimitriadis, P.; Iliopoulou, T.; Ioannidis, R.; Karakatsanis, G.; Efstratiadis, A.; Mamasis, N.; Tomani, R.; Chardavellas, E.; et al. A preliminary stochastic analysis of the uncertainty of natural processes related to renewable energy resources. *Adv. Geosci.* **2018**, *45*, 193–199. https://doi.org/10.5194/ADGEO-45-193-2018.
12. Fotopoulou, M.; Tsekouras, G.; Rakopoulos, D.; Kanelios, F.; Kontargyri, V. Investment planning optimization for energy communities with photovoltaic and storage. *IEEE Access* **2026**, *14*, 98275–98294. https://doi.org/10.1109/ACCESS.2026.3707056.
13. Iheanetu, K.J. Solar photovoltaic power forecasting: A review. *Sustainability* **2022**, *14*, 17005. https://doi.org/10.3390/SU142417005.
14. Yang, D.; Wang, W.; Gueymard, C.; Hong, T.; Kieissl, J.; Huang, J.; Perez, M.; Perez, R.; Bright, J.; Xia, X.; et al. A review of solar forecasting, its dependence on atmospheric sciences and implications for grid integration: Towards carbon neutrality. *Renew. Sustain. Energy Rev.* **2022**, *161*, 112348. https://doi.org/10.1016/j.rser.2022.112348.
15. Li, B.; Zhang, J. A review on the integration of probabilistic solar forecasting in power systems. *Sol. Energy* **2020**, *210*, 68–86. https://doi.org/10.1016/J.SOLENER.2020.07.066.
16. ECMWF. *IFS Documentation*; European Centre for Medium-Range Weather Forecast: Shinfield Park, Reading, UK, 2026. Available online: https://www.ecmwf.int/en/publications/ifs-documentation (accessed on 16 November 2026).
17. Prill, F.; Reinert, D.; Rieger, D.; Zängl, G. *ICON Tutorial*; Deutscher Wetterdienst: Offenbach am Main, Germany 2025; 296p. https://doi.org/10.5676/DWD_pub/nwv/icon_tutorial2025.
18. Müller, W.A.; Früh, B.; Kom, P.; Potthast, R.; Baehr, J.; Bettems, J.M.; Bölöni, G.; Brienen, S.; Fröhlich, K.; Helmert, K.; et al. ICON: Toward vertically integrated model configurations for numerical weather prediction, climate predictions, and projections. *Bull. Amer. Meteorol. Soc.* **2025**, *106*, E1017–E1031. https://doi.org/10.1175/BAMS-D-24-0042.1.
19. Monk, K.; Guerette, E.A.; Walsh, C.P.; Silver, J.D.; Emmerson, K.M.; Utembe, S.R.; Zhang, Y.; Griffiths, A.D.; Chang, L.T.-C.; Duc, H.N. Evaluation of regional air quality models over Sydney and Australia: Part 1–meteorological model comparison. *Atmosphere* **2019**, *10*, 374. https://doi.org/10.3390/ATMOS10070374.
20. Cheung, K.K.W.; Ji, F.; Nishant, N.; Herold, N.; Cook, K. Evaluation of convective environments in the NARCliM regional climate modeling system for Australia. *Atmosphere* **2023**, *14*, 690. https://doi.org/10.3390/atmos14040690.
21. Cheung, K.K.W.; Yeasmin, A.; Monk, K.; Kong, J.; Jiang, N.; Ji, F.; Chang, L.T.-C.; Wahiduzzaman, M.; Duc Nguyen, H.; Merched, A.; et al. Evaluation of an Australian regional climate modeling system for air-quality application. *Climate* **2026**, *14*, 54 https://doi.org/10.3390/CLI14020054.
22. Yue, X.; Tang, X.; Hu, B.; Chen, K.; Wu, Q.; Kong, L.; Wu, H.; Wang, Z.; Zhu, J. Evaluation of the simulation performance of WRF-Solar for a summer month in China using ground observation network data. *Atmos. Ocean. Sci. Lett.* **2025**, *18*, 100532. https://doi.org/10.1016/J.AOSL.2024.100532.
23. Zhang, H.; Li, L.; Zhang, X.; Liu, S.; Zheng, Y.; Gui, K.; Ma, J.; Che, H. Assessment of WRF-Solar and WRF-Solar EPS radiation estimation in Asia using the geostationary satellite measurement. *Remote Sens.* **2025**, *17*, 3970. https://doi.org/10.3390/rs17243970.

Disclaimer/Publisher's Note: The statements, opinions and data contained in all publications are solely those of the individual author(s) and contributor(s) and not of MDPI and/or the editor(s). MDPI and/or the editor(s) disclaim responsibility for any injury to people or property resulting from any ideas, methods, instructions or products referred to in the content.